Journal of
Manufacturing and
Materials Processing

*Article*

# Effect of Al/Cu Ratio on Microstructure and High-Temperature Oxidation Resistance of $Al_xCoCrCu_yFeNi$ High-Entropy Alloy Coatings

**Ling Zhou, Hongxi Liu *, Qinghua Zhang, Jiazhu Liang, Yuanrun Peng, Xuanhong Hao, Chen Yang, Yaxia Liu and Yueyi Wang**

Faculty of Materials Science and Engineering, Kunming University of Science and Technology, Kunming 650093, China; 17869418798@163.com (L.Z.); zqhzam1001@163.com (Q.Z.); 20222130076@stu.kust.edu.cn (J.L.); pyr6798@163.com (Y.P.); hxh_instinct@163.com (X.H.); 20233130007@stu.kust.edu.cn (C.Y.); 20212130082@stu.kust.edu.cn (Y.L.); wyy_0710@126.com (Y.W.)
* Correspondence: piiiliuhx@sina.com or liuhx@kust.edu.cn

**Abstract:** To improve high-temperature oxidation resistance for Ti6Al4V alloy, $Al_xCoCrCu_y$-FeNi (x = 0, 0.3, 0.5, 0.7, 1.0; y = 1.0, 0.7, 0.5, 0.3, 0, x + y = 1.0) high-entropy alloy (HEA) coatings were prepared on the Ti6Al4V alloy substrate by a laser cladding technique. The results show that the coatings were mainly composed of FCC, BCC, and Ti-rich phases. Severe segregation of the Cu element occurred in the CoCrCuFeNi HEA coatings as a Cu-rich phase (FCC2). The Cu-rich phases decreased with a decreasing Cu content and completely disappeared until the Al content reached 1.0. The microhardnesses of the $Cu_{1.0}$, $Cu_{0.7}Al_{0.3}$, $Cu_{0.5}Al_{0.5}$, $Cu_{0.3}Al_{0.7}$, and $Al_{1.0}$ HEA coatings were 2.01, 2.06, 2.08, 2.09, and 2.11 times that of the substrate, and compared with those of a Ti6Al4V alloy substrate, the oxidation rates of the HEA coatings decreased by 55%, 51%, 47%, 42%, and 35%, respectively. The surface oxides of the five coatings were mainly composed of CuO, $TiO_2$, $Fe_3O_4$, $Cr_2O_3$, and $Al_2O_3$. The increase in the Al content promoted the generation of $Al_2O_3$ film and $Cr_2O_3$ on the surfaces of the coatings, which significantly improved the high-temperature antioxidant performance of the high-entropy alloy coatings for 50 h at 800 °C. When x = 1.0, the coating showed the best high-temperature antioxidant performance.

**Keywords:** high-entropy alloy; laser cladding; high-temperature oxidation resistance; microstructure; Ti6Al4V alloy

Academic Editor: Shuting Lei

Received: 20 November 2024
Revised: 16 December 2024
Accepted: 1 January 2025
Published: 5 January 2025

**Citation:** Zhou, L.; Liu, H.; Zhang, Q.; Liang, J.; Peng, Y.; Hao, X.; Yang, C.; Liu, Y.; Wang, Y. Effect of Al/Cu Ratio on Microstructure and High-Temperature Oxidation Resistance of $Al_xCoCrCu_yFeNi$ High-Entropy Alloy Coatings. *J. Manuf. Mater. Process.* **2025**, *9*, 13. https://doi.org/10.3390/jmmp9010013

## 1. Introduction

Titanium alloys are widely used as important structural materials in fields such as aerospace, petrochemical, automobile, biomedicine, and architectural decoration due to their low density, high specific strength, excellent corrosion resistance, and biocompatibility [1]. Ti6Al4V alloy, as an important titanium alloy material, has attracted much attention. However, in some specific application scenarios, the relatively weak hardness and high-temperature oxidation resistance make Ti6Al4V alloy fail easily during service in extreme environments. Therefore, in order to solve this problem, many researchers are committed to exploring new surface treatment technologies [2–4].

Nowadays, the main surface modification methods include thermal spraying technology, vapor deposition technology, electrochemical surface modification, surface nanocrystallization, ion implantation, and laser cladding technology [5–12]. As an advanced material surface modification technology, laser cladding (LC) has the advantages of a high bonding strength between the coating and the substrate, a small heat-affected zone, and precise control of the composition of the coating, which can effectively reduce the impact on the properties of the substrate [13–15]. In recent years, many researchers have improved the surface properties of titanium alloys using laser cladding technology, and the material systems that have been investigated include Ni-based alloy systems [16,17], metal–ceramic composite systems [18–21], and rare earth element modification systems [22,23]. Unfortunately, in the material system described above, due to the large differences in the coating and the substrate's physical and chemical properties, the combination of the coating and the substrate is often not strong enough, and these materials are less elemental, easily forming a large number of intermetallic brittle phases, resulting in a reduction in toughness. Even some of the material preparation costs are high, and the process is complex and difficult to mass produce. Additionally, there are other factors affecting the effectiveness of the surface engineering. And it is difficult to meet the practical application requirements.

High-entropy alloys (HEAs), as a new type of alloy material, have a unique composition that imparts a high entropy effect, a hysteresis diffusion effect, a lattice distortion effect, and a "cocktail" effect, and it possesses high thermal stability [24–27]. The high entropy of mixing encourages the alloys to tend to form simple solid solutions, such as face-centered cubic (FCC), body-centered cubic (BCC), and hexagonal close-packed (HCP) [28,29]. Due to their unique microstructure and the synergistic effect between multiple elements, HEAs have excellent properties, such as high strength, corrosion resistance, and high-temperature resistance. CoCrFeNi high-entropy alloy has attracted extensive research interest due to its good toughness, which is mainly attributed to its single face-centered cubic (FCC) structure [30]. This structure can form a uniform, dense coating on the surface of the substrate and form a good bond, avoiding the brittle fracture that tends to occur in laser cladding coating materials. Compared with the traditional alloy coatings consisting of only one or two elements, the unique multi-element mixed structure of a CoCrFeNi high-entropy alloy coating makes dislocation movement more difficult. This unique microstructure impedes dislocation movement to a greater extent, thereby minimizing wear and deformation and enhancing the mechanical properties of the coating. It tends to form a simple multi-component solid-solution structure with a relatively single-phase composition and uniform element distribution, ensuring the consistency and stability of its performance over an extended period of use. Through the modulation of the types and amounts of elements, a diverse range of performance characteristics can be achieved, catering to the specific and individualized demands of various engineering applications in terms of material performance. The synergistic interaction among its multiple elements frequently endows it with performance superiority over traditional alloy coatings, consequently attracting more extensive attention and research efforts [31–33]. However, the lack of hardness and oxidation resistance of the CoCrFeNi high-entropy alloy poses a challenge for further use in high-temperature environments. It has been shown that the element Al can have a significant effect on the hardness and high-temperature oxidation behavior of HEAs, and increasing the amount of Al can improve the oxidation resistance of HEAs through the formation of an $Al_2O_3$ oxide layer [34–36]. Huang [37] prepared a TiVCrAlSi HEA coating on a Ti6Al4V alloy by laser cladding and found that the microstructure of the coating consisted of $(Ti, V)_5Si_3$ and BCC solid solutions. The $SiO_2$, $Cr_2O_3$, $TiO_2$, and $Al_2O_3$ and a small quantity of $V_2O_5$ produced during the oxidation process of the laser-clad TiVCrAlSi coating could effectively enhance the oxidation resistance of a Ti6Al4V alloy in the air at 800 °C. Zhang [38] prepared a TiAlNiSiV HEA coating with a BCC phase structure on the surface of a Ti6Al4V alloy by laser cladding, and the results showed that the hardness of the TiAlNiSiV HEA coating was $1151\sim1357$ $HV_{1.0}$, which was $4\sim6$ times that of the substrate, and the wear resistance of the TiAlNiSiV HEA coating at 800 °C was four times that of the substrate. Geng [39] prepared $(AlCu)_{3.5}$CoCrNiFe and $(AlCu)_{3.5}$CoCrNiTi HEA coatings on an AZ91 magnesium alloy using a laser cladding technique; both coatings were BCC and FCC phases. Their microhardnesses were 642.1 $HV_{1.0}$ and 656.2 $HV_{1.0}$, respectively, which were about 9 times higher than that of the AZ91 substrate (71.9 $HV_{1.0}$). The $TiO_2$ produced in $(AlCu)_{3.5}$CoCrNiTi formed an oxide film during the oxidation process, resulting in excellent oxidation resistance of the substrate. It can be seen that the application of HEAs makes the surface properties of materials significantly improved. However, an excess of Al may cause the alloy to become too hard and brittle, thereby reducing its toughness and plasticity, which in turn negatively impacts its mechanical properties. The composition of the phases can be controlled to increase the toughness of the alloy by the addition of elements with good plasticity (such as Cu) and by adjusting the ratio of the elements.

In this study, Al and Cu elements were added to the CoCrFeNi alloy system. The addition of the Al element can effectively improve the microhardness and oxidation resistance of the coating but also make the coating brittle. In contrast, the introduction of the Cu element can enhance the plasticity of the coating. This paper innovatively adjusted the ratio of Al/Cu at the same time, allowing for the optimization of the coating's morphology and performance. The $Al_xCoCrCu_yFeNi$ (x = 0, 0.3, 0.5, 0.7, 1.0; y = 1.0, 0.7, 0.5, 0.3, 0, x + y = 1) HEA coatings were prepared on the surface of a Ti6Al4V alloy by laser cladding technology. The effects of varying the Al and Cu contents on the microstructure, microhardness, and high-temperature oxidation resistance were systematically analyzed to further elucidate the underlying principles.

## 2. Materials and Methods

### 2.1. Experimental Materials and Preparation of Coating

The substrate in this study is a Ti6Al4V alloy in a rolling state with a dual-phase $\alpha + \beta$ structure (sample size 150 mm × 15 mm × 10 mm). One side of each substrate sample was polished with 240-grit and 400-grit SiC abrasive paper to remove surface oxides and contaminants, which also helped reduce laser reflection. The samples were then thoroughly cleaned in absolute ethanol to eliminate oil, rust, and other impurities from the surface. Before laser cladding, the sample was dried in an electric box at 80 °C for 2 h.

Commercially available Al, Cu, CoCrFeNi alloy spherical powder (Beijing Yanbang Metal Materials Co., Ltd., China) with a purity of more than 99.9% (particle size from 15 μm to 53 μm) was selected as the raw material. The mixed powders were weighed according to the atomic ratio of $Al_xCoCrCu_yFeNi$ (x = 0, 0.3, 0.5, 0.7, 1.0; y = 1.0, 0.7, 0.5, 0.3, 0, x + y = 1). The specific alloy powder ratios are shown in Table 1. An MSK-SFM-1S-type high-flux planetary ball mill was used to mix the powders in dry grinding mode. To prevent damage to the sphericity of the initial powder and avoid oxidation during the ball milling process. We used the following parameters: a speed of 120 rpm, milling times of 8 h, and a ball-to-power ratio of 4: 1. After ball milling, the mixed powders were dried at 60~80 °C for 1~2 h. The SEM images and EDS elemental distribution of the raw powders are shown in Figure 1a-g. SEM and EDS analysis results indicate that the mixed powders are relatively uniform, with good sphericity, show no obvious fragmentation, and do not exhibit agglomeration or oxidation. Figure 1h shows the XRD pattern of the $Al_{0.5}CoCrCu_{0.5}FeNi$ power, which reveals no formation of new phases.

The mixture powder was preset on the Ti6Al4V alloy plate surface with $CH_3CH_2OH$ organic binder (thickness 1 mm) and then dried in an electric oven at 80 °C for 5 h. A fiber laser (XL-F1500) with a power output of 1500 W was used to prepare $Al_xCoCrCu_yFeNi$ HEA coatings on the Ti6Al4V alloy surface. After conducting several orthogonal experiments, the optimal processing parameters for this study were determined as follows: laser power of 1100 W, laser scanning speed of 300 $mm \cdot min^{-1}$, circular spot diameter of 4 mm, and defocus of 13 mm. To prevent oxidation, Ar was used as the protection gas (99.99% purity, blowing to one side of the molten pool), with a gas flow rate of 15 L·min$^{-1}$.

**Table 1.** Composition of the mixed powder (at. %).

| Groups | Ratios | Al/ Cu | Simplified |
|---|---|---|---|
| 1 | CoCrCuFeNi | 0:1 | $Cu_{1.0}$ |
| 2 | $Al_{0.3}CoCrCu_{0.7}FeNi$ | 0.3:0.7 | $Cu_{0.7}Al_{0.3}$ |
| 3 | $Al_{0.5}CoCrCu_{0.5}FeNi$ | 0.5:0.5 | $Cu_{0.5}Al_{0.5}$ |
| 4 | $Al_{0.7}CoCrCu_{0.3}FeNi$ | 0.7:0.3 | $Cu_{0.3}Al_{0.7}$ |
| 5 | AlCoCrFeNi | 1:0 | $Al_{1.0}$ |

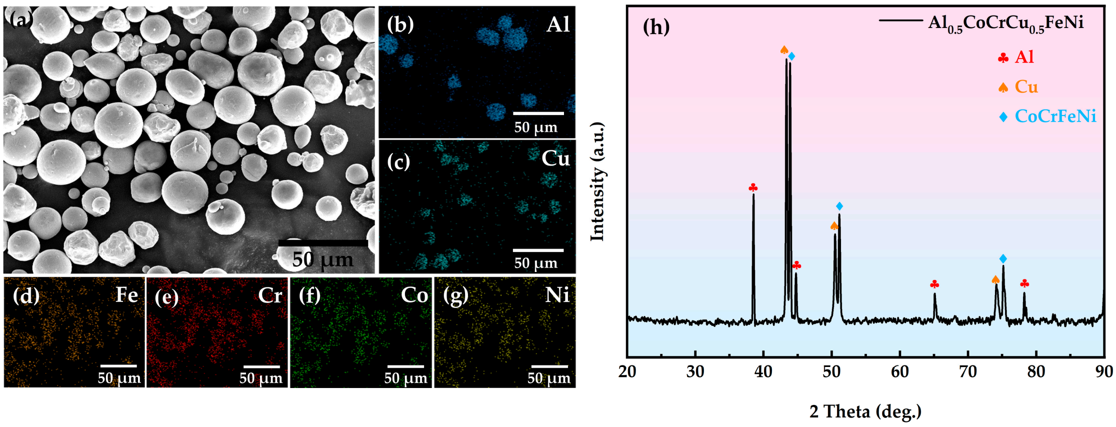

**Figure 1.** SEM image and EDS elemental distribution of the raw powder: (**a**) SEM image of the mixed powder; (**b**–**g**) EDS elemental distribution of the powder; (**h**) XRD pattern of $Al_{0.5}CoCrCu_{0.5}FeNi$ power.

### 2.2. Microstructure Characterization

The prepared high-entropy alloy coatings were cut into rectangular samples with the size of 20 mm × 10 mm × 10 mm using electric discharge wire cutting technology. The coating section of each sample was polished with 240, 600, 800, 1200, and 2000 mesh sandpapers to remove oil stains and oxides on the surface until smooth. The samples were then polished to a mirror finish using a 0.12 µm silica polishing liquid, ensuring the surface had no obvious scratches, and finally with anhydrous ethanol ultrasonic cleaning.

The microstructure of the laser cladding coating was analyzed by an EMPYREAN-type X-ray diffractometer (XRD) from Malvern-Panaco, Netherlands, with a Cu cathode target and $K\alpha$ line wavelength of 1.5406 Å, working voltage of 40 kV, and working current of 30 mA. The scan was conducted with a step size of 5°·min$^{-1}$over a $2\theta$ range of 20° to 90° (CSM, continuous scan mode). Scanning electron microscopy (SEM; TESCAN VEGA 3., Czech Republic; HV: 20.0 kV) and its energy dispersive X-ray spectrometer (EDS) were used to analyze the phase microstructure, micro-morphology, and elemental distribution of the cross-sectional coating samples.

### 2.3. Performance Tests

The surface of the laser cladding coating sample was initially pre-treated by sanding and polishing until free of scratches and ultrasonically cleaned with alcohol. The microhardness of the laser cladding coating sample was tested using a 3S-1000QZD-type automatic Vickers hardness tester (Zhejiang Sansi Yongheng Technology Co., Ltd., China), with a load of 5 N and a dot placed at intervals of 0.2 mm from the surface of the laser cladding coating towards the substrate for 15 s.

The high-temperature oxidation resistance of the coatings and the substrate was evaluated using a GSL-1700X-type tube resistance furnace (Shenyang Kejing Automation Equipment Co., Ltd., China). The oxidation process followed a cyclic pattern at a constant temperature of 800 °C, with a total oxidation duration of 50 h. The coatings and the Ti6Al4V alloy substrate were taken out at 5 h, 10 h, 15 h, 30 h, and 50 h. After natural cooling, the oxidation weight gain of both the coatings and the Ti6Al4V alloy substrate was measured. The oxidation kinetics curve was subsequently plotted. The oxidation morphology and the oxides formed on the oxidized surfaces of the coatings and the Ti6Al4V alloy substrate were examined using a scanning electron microscope (SEM) equipped with energy dispersive spectrometer (EDS), and the oxidation mechanism of the coatings was analyzed.

## 3. Results and Discussion

### *3.1. XRD Phase Analysis and Microstructure Analysis*

Figure 2 presents the X-ray diffraction (XRD) patterns of the $Al_xCoCrCu_yFeNi$ (x = 0, 0.3, 0.5, 0.7, 1.0; y = 1.0, 0.7, 0.5, 0.3, 0) HEA coatings with varying Al and Cu ratios. The microstructure of the coatings was composed of FCC, BCC, and a small amount of Laves phases. The FCC phase includes the matrix phase (FCC1) and the Cu-rich phase (FCC2), while the BCC phase is primarily Fe-Cr-rich and the hard Laves phase is rich in Ti. It can be seen that three prominent diffraction peaks appear at 43.12°, 63.32°, and 80.10°, corresponding to the main FCC solid solution phase, while a second set of peaks at 44.15°, 64.39°, and 81.80° corresponds to the BCC phase. This is attributed to the more constituent elements and the close atomic percentage of each element in the HEA, resulting in a higher mixing entropy and a lower Gibbs free energy in the system, which promotes the formation of random disordered solid solution phases with simple and stable microstructures [40]. It can be clearly seen that in addition to the main peaks, several smaller peaks are observed in the XRD patterns. According to the literature [41], and matching with PDF card data, these are attributed to Ti-rich Laves-reinforced phases. Furthermore, when the Cu content is 1.0, Cu-rich phases are detected at diffraction peaks of 43.12°, 50.08°, and 89.29°, but these peaks disappear when the Cu content is reduced to 0.3. This may be due to the low Cu content at which the X-ray diffraction cannot detect these phases. With the decrease in the Cu content, the intensity of the FCC peaks gradually diminishes. Simultaneously, with the increase in the Al content and the decrease in the Cu content, the intensity of the Laves phase diffraction peaks also decreases.

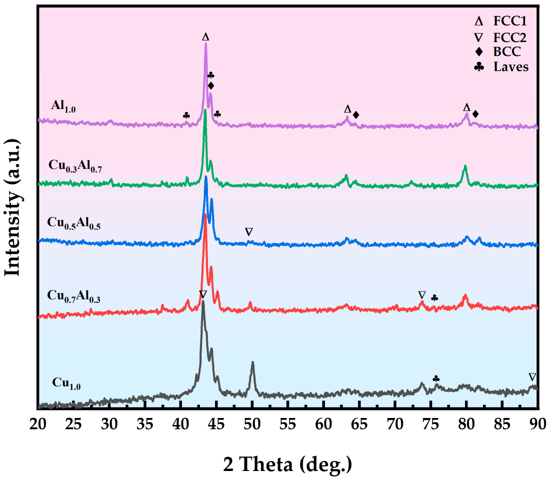

**Figure 2.** XRD patterns of the $Al_xCoCrCu_yFeNi$ HEA coatings.

The cross-sectional microscopic morphology and the EDS line scanning distribution curves of different elements along the cross-section of the $Al_{0.7}CoCrCu_{0.3}FeNi$ coating are shown in Figure 3a. According to the literature [42], the dilution rate is calculated using the following equation (Equation (1)):

$$\lambda = \frac{h}{H + h} \times 100\% \tag{1}$$

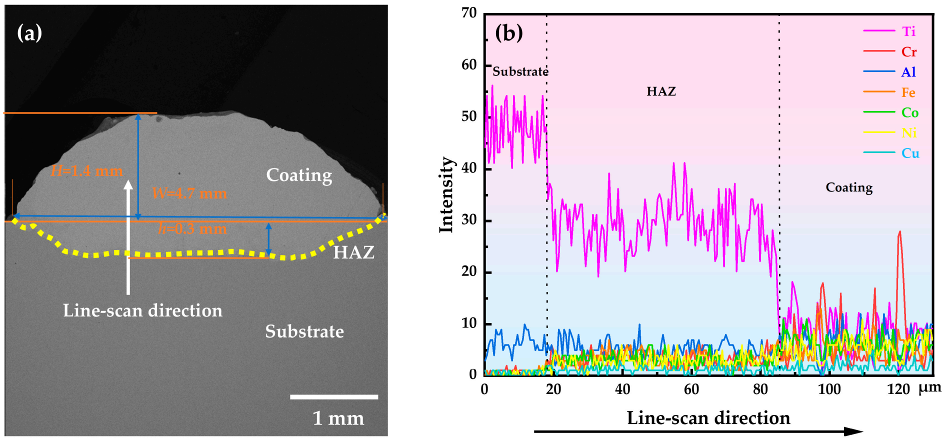

**Figure 3.** Macroscopic cross-section morphology of the $Al_{0.7}CoCrCu_{0.3}FeNi$ HEA coating: (**a**) The cross-sectional morphology; (**b**) the EDS line scanning distribution curves of the different elements along the cross-section.

According to the data shown in Figure 3a, the dilution rate of the coating is determined to be 17.6%. As indicated by the EDS line scanning results in Figure 3b, element diffusion is observed between the coating and the substrate. This demonstrates a strong metallurgical bond between the coating and the substrate. Generally, dilution is a critical parameter in laser cladding HEA coating. A low dilution rate in HEA coating may lead to insufficient melting and poor formability, while an excessively high dilution rate can alter the microstructure and properties of the coating. An optimal dilution rate enhances the bond strength between the coating and the substrate, results in a more uniform coating structure, and better preserves the original characteristics of the HEA, along with the stability of its structure [43,44].

Figure 4 shows the cross-sectional SEM images of the upper and middle regions of the coatings. It can be observed that the coating exhibits a typical dendrite microstructure. When the Cu content is 1.0, a light-gray microstructure is present in the inter-dendritic regions at the top of the coating, while a butterfly-like dark-gray microstructure is observed within the dendrites. With the decreases in the Cu content and the increases in the Al content, the grains evolve from a cellular structure to a chrysanthemum-like shape and ultimately to petal-like equiaxed crystals, and gradually decrease with a small amount of dispersed black petal-like or granular precipitates. The dark-grey microstructure in the dendrites and the light-grey microstructure in the inter-dendrites show that the grain size decreases from the top to the bottom of the coating, accompanied by a reduction in the size of the black granular precipitates. In addition, as shown in Figure 4a–d, white precipitates accumulate at the grain boundaries, with their content decreasing progressively. Due to the high mixing entropy effect [45], no intermetallic compounds were found in the middle region of the coatings, which promoted the dissolution of the main components and inhibited the precipitation of the intermetallic compounds.

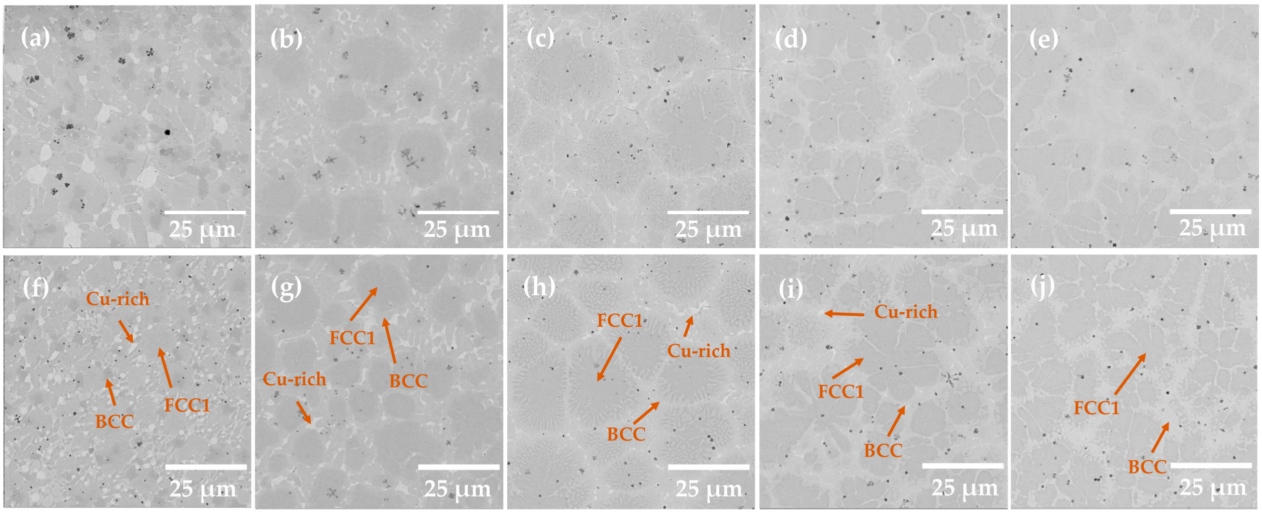

**Figure 4.** Microstructure of top and central coatings of $Al_xCoCrCu_yFeNi$ HEA coatings: (**a**,**f**) $Cu_{1.0}$; (**b**,**g**) $Cu_{0.7}Al_{0.3}$; (**c**,**h**) $Cu_{0.5}Al_{0.5}$; (**d**,**i**) $Cu_{0.3}Al_{0.7}$; (**e**,**j**) $Al_{1.0}$; (**a**–**e**) top of coating; (**f**–**j**) center of coating.

To further analyze the distribution of different elements, EDS scanning was performed, and the results are shown in Figure 5. Combined with the previously discussed XRD results, it is evident that the dark-gray microstructure in the dendrites corresponds to the FCC phase, while the light-gray microstructure in the inter-dendritic regions corresponds to the BCC phase. Due to the mutual dilution between the coating and the substrate, the Ti element from the Ti6Al4V alloy substrate is continuously diffused into the coating during the laser cladding process, leading to an increased Ti element in the coating. This promotes the formation of the FCC phase enriched in Al-Co-Ni-Ti, which grows into equiaxed crystals. During the solidification process, the content of Fe and Cr elements in the liquid molten pool gradually increases until it reaches the maximum solubility limit of the liquid metal, at which point these elements precipitate as an alloy phase. Since Cr has the highest melting point, it is preferred to precipitate to form a Fe-Cr-rich BCC phase. At the same time, the atomic radius of Ti is significantly larger than that of other elements, and the mixing enthalpy is low, resulting in the segregation of Ti elements in the coating and the formation of dispersed Laves phases. The EDS analysis results at different locations in Figure 5 are provided in Table 2. The black petal-like precipitates and the black particles dispersed in the coating are Ti-rich Laves phases.

**Table 2.** EDS results of areas in Figure 5.

| Points | Elements (at. %) | | | | | | |
|---|---|---|---|---|---|---|---|
| | Al | Co | Cr | Cu | Fe | Ni | Ti |
| 1 | - | 14.5 | 10.6 | 10.4 | 11.5 | 18.0 | 35.0 |
| 2 | 8.1 | 10.8 | 3.9 | 3.9 | 5.8 | 10.3 | 57.3 |
| 3 | 14.0 | 14.9 | 7.4 | 3.3 | 9.0 | 15.1 | 36.4 |
| 4 | 29.2 | 11.0 | 6.9 | 2.1 | 7.7 | 10.2 | 32.8 |
| 5 | 22.7 | 13.6 | 6.0 | - | 8.0 | 12.2 | 37.4 |

Based on the above-mentioned analysis, it can be seen that the light-gray area of the $Cu_{1.0}$ coating corresponds to the Co-Ni-Ti-rich FCC phase, while the BCC phase in the inter-dendritic regions is Fe-Cr-rich and the white microstructure at the grain boundaries is the Cu-rich phase. During the process of cladding, the Ti atom, with its large atomic radius and slow diffusion rate, exhibits negative mixing enthalpy with Co and Ni elements, promoting the formation of $Co_3Ti$ or $Ni_3Ti$ phases. This, in turn, facilitates the aggregation of Fe and Cr elements into the dendrites. The mixing enthalpy values for different atomic pairs between the elements are listed in Table 3. The Cu element has a positive mixing enthalpy and a lower melting point, resulting in a weak affinity with other elements and low bonding strength. As a result, the Cu element does not readily form solid solutions with other elements and is extruded to the grain boundaries, forming Cu-rich phases. This process leads to a reduction in the grain size. In the $Cu_{0.7}Al_{0.3}$, $Cu_{0.5}Al_{0.5}$, $Cu_{0.3}Al_{0.7}$, and $Al_{1.0}$ coatings, chrysanthemum-like dendrites and petal-like equiaxed dendrites are observed in the FCC phase, which is rich in Al-Co-Ni-Ti, while the light-gray microstructure in the BCC phase is rich in Fe-Cr. The white monomer at the grain boundaries in $Cu_{0.7}Al_{0.3}$, $Cu_{0.5}Al_{0.5}$, and $Cu_{0.3}Al_{0.7}$ are also Cu-rich phases. With the decrease in the Cu content, the Cu-rich phase at the grain boundaries significantly decreases and eventually disappears when the Al content reaches 1.0, along with the disappearance of the FCC2 phase. With the increase in the Al content, the negative mixing enthalpy between Ti and Al causes the FCC1 phase to transition from being Co-Ni-Ti-rich to $AlNi_2Ti$- or $AlCo_2Ti$-rich.

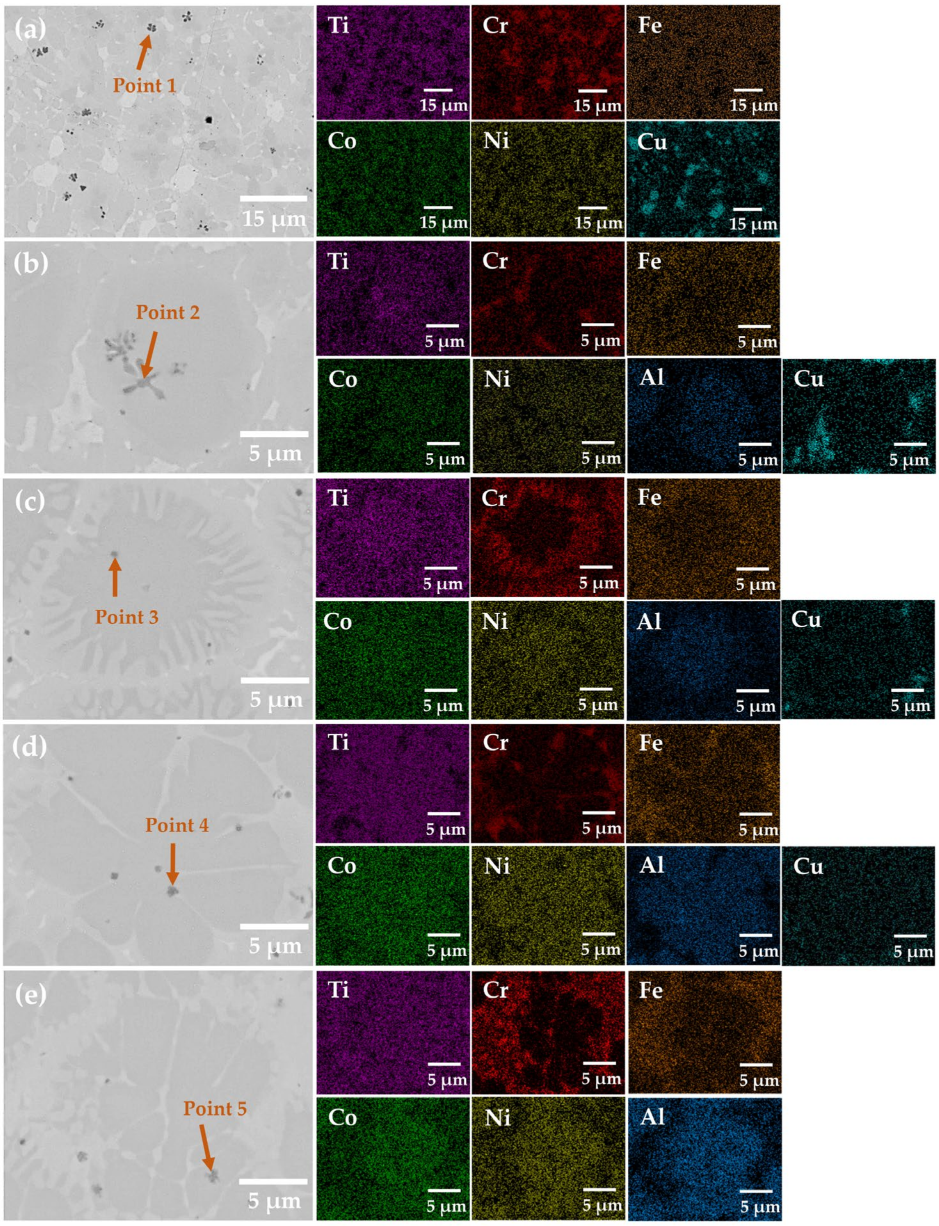

**Figure 5.** Microstructure of $Al_xCoCrFeCu_yNi$ HEA coatings: (**a**) $Cu_{1.0}$; (**b**) $Cu_{0.7}Al_{0.3}$; (**c**) $Cu_{0.5}Al_{0.5}$; (**d**) $Cu_{0.3}Al_{0.7}$; (**e**) $Al_{1.0}$.

**Table 3.** $\Delta H_{mix}$ enthalpy of mixing of different atomic pairs.

| Elements | Enthalpy (kJ·mol$^{-1}$) | | | | | | |
|---|---|---|---|---|---|---|---|
| | **Al** | **Co** | **Cr** | **Fe** | **Ni** | **Cu** | **Ti** |
| Al | - | −19 | −10 | −11 | −22 | −1 | −30 |
| Co | - | - | −4 | −1 | 0 | 6 | −28 |
| Cr | - | - | - | −1 | −7 | 12 | −7 |
| Fe | - | - | - | - | −2 | 13 | −17 |
| Ni | - | - | - | - | - | 4 | −35 |
| Cu | - | - | - | - | - | - | 4 |
| Ti | - | - | - | - | - | - | - |

### *3.2. Microhardness of the Coating and the Ti6Al4V Alloy Substrate*

The microhardness distribution curves and the average microhardness values of the HEA coatings and the Ti6Al4V alloy substrate are shown in Figure 6. As shown in Figure 6a, the microhardness increases significantly from the substrate to the surface of the coating. Figure 6b displays the average microhardness values of the Ti6Al4V alloy substrate and the $Al_xCoCrCu_yFeNi$ (x = 0, 0.3, 0.5, 0.7, 1.0; y = 1.0, 0.7, 0.5, 0.3, 0, x + y = 1) HEA coatings, which are as follows: 344.76 $HV_{0.5}$, 694.70 $HV_{0.5}$, 711.48 $HV_{0.5}$, 716.19 $HV_{0.5}$, 720.71 $HV_{0.5}$, and 727.61 $HV_{0.5}$. The average microhardness of the HEA coatings is 2.01, 2.06, 2.08, 2.09, and 2.11 times that of the Ti6Al4V alloy substrate, respectively. During the process of laser cladding, due to dilution between the Ti6Al4V alloy substrate and the coating, the Ti element from the substrate diffuses into the coating, resulting in an increase in the Ti element content in the coating. The large atomic radius of Ti enhances the lattice distortion effect within the coating, which promotes the segregation of BCC phases (Cr-Fe phase) and contributes to solid solution strengthening. In addition, the low mixing enthalpy of Ti with other elements further promotes the formation of the reinforced phase. Ti combines with other elements in the coating to form hard Laves phase and Ti-rich particles, which are dispersed throughout the coating. As a result of precipitation strengthening, the coating is strengthened, and the hardness is significantly increased. In addition, the large atomic radius of Al, combined with the increasing Al content, leads to greater lattice distortion, which impedes dislocation movement, resulting in a stronger solid solution strengthening effect. In summary, the microhardness of the coating is significantly enhanced due to the lattice distortion caused by the incorporation of elements with large atomic radii, which induces solid solution strengthening. The diffusion of the Ti element from the substrate into the coating also promotes the precipitation of the hard phases, contributing to the precipitation-strengthening effect.

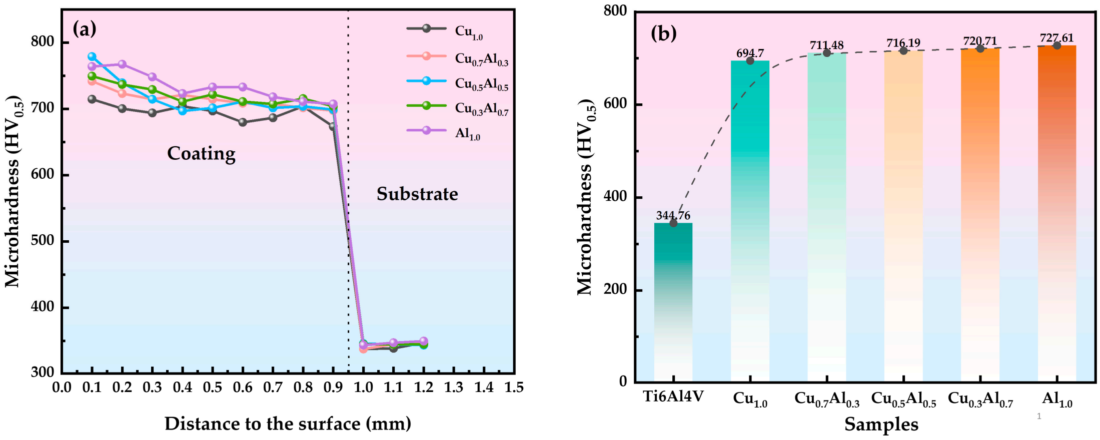

**Figure 6.** Microhardness results of the coatings and Ti6Al4V alloy: (**a**) microhardness distribution; (**b**) average microhardness.

### 3.3. Oxidation Behavior

The oxidation resistance of the Ti6Al4V alloy and HEA coatings was evaluated at 800 °C for a total duration of 50 h, with measurements taken at intervals of 5 h, 10 h, 15 h, 30 h, and 50 h. Figure 7a shows the oxidation mass gain per unit area for the Ti6Al4V alloy substrate and the $Al_xCoCrCu_yFeNi$ (x = 0, 0.3, 0.5, 0.7, 1.0; y = 1.0, 0.7, 0.5, 0.3, 0, x + y = 1) HEA coatings. The results indicate that the oxidation mass gain for the HEA coatings and Ti6Al4V alloy substrate are 0.156 $mg \cdot mm^{-2}$, 0.143 $mg \cdot mm^{-2}$, 0.133 $mg \cdot mm^{-2}$, 0.118 $mg \cdot mm^{-2}$, 0.098 $mg \cdot mm^{-2}$, and 0.283 $mg \cdot mm^{-2}$, respectively. Compared to the Ti6Al4V alloy, the oxidation rates of the $Cu_{1.0}$, $Cu_{0.7}Al_{0.3}$, $Cu_{0.5}Al_{0.5}$, $Cu_{0.3}Al_{0.7}$, and $Al_{1.0}$ HEA coatings decreased by 55%, 51%, 47%, 42%, and 35%, respectively. The oxidation mass gain of the HEA coatings is significantly lower than that of the Ti6Al4V alloy substrate. In addition, the addition of Al content improves the oxidation resistance of the $Al_xCoCrCu_yFeNi$ HEA coatings. Before 15 h, all of the HEA coatings exhibit a rapid initial increase in oxidation mass gain, which is attributed to the rapid oxide growth at the early stages of the oxidation process [46]. During this stage, the initial oxide layer nucleates and grows on the surface, primarily consisting of less protective oxides. Over time, the oxidation mass gain of the HEA coating increases slowly, whereas the oxidation mass gain of the Ti6Al4V alloy substrate increases rapidly. This difference in behavior suggests that the formation of the oxide layer is controlled by the outward diffusion of the constituent elements with high diffusion coefficients. To better understand the oxidation kinetics of the $Al_xCoCrCu_yFeNi$ HEA coatings, a power function [47,48] (Equation (2)) was used to fit the oxidation mass gain as a function of time:

$$\left(\frac{\Delta m}{A}\right)^2 = k_p \times t \tag{2}$$

where $\Delta m$—the oxidation mass gain (mg), A—the surface area ($mm^2$), $k_p$—the parabolic oxidation rate constant, and $t$—the oxidation time (h) at high temperatures.

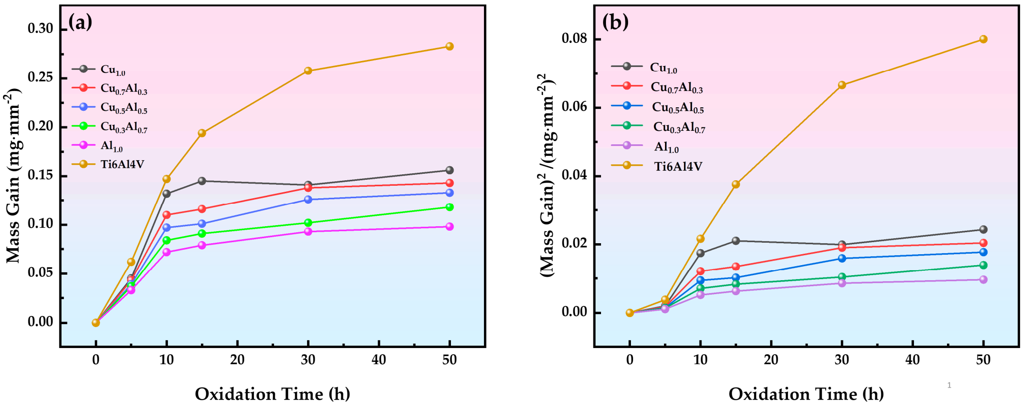

**Figure 7.** Oxidation kinetics curves of the $Al_xCoCrCu_yFeNi$ HEA coatings and Ti6Al4V alloy at 800 °C: (**a**) original curves; (**b**) linear fit curves.

Figure 7b shows the relationship between the square of the mass gain per unit area and oxidation time. In addition, the oxidation rate constant $k_p$ values were calculated according to Equation (2). The oxidation rate constants $k_p$ of each coating and the Ti6Al4V alloy substrate after oxidation at 800 °C for 50 h are $4.8672 \times 10^{-4}$ $mg^2 \cdot mm^{-4} \cdot h^{-1}$, $4.0898 \times 10^{-4}$ $mg^2 \cdot mm^{-4} \cdot h^{-1}$, $3.5378 \times 10^{-4}$ $mg^2 \cdot mm^{-4} \cdot h^{-1}$, $2.7848 \times 10^{-4}$ $mg^2 \cdot mm^{-4} \cdot h^{-1}$, $1.9208 \times 10^{-4}$ $mg^2 \cdot mm^{-4} \cdot h^{-1}$, and $16.0185 \times 10^{-4}$ $mg^2 \cdot mm^{-4} \cdot h^{-1}$, respectively. It can be seen that the AlCoCrFeNi HEA coating exhibited the best oxidation resistance. This shows that the high-entropy alloy coatings can significantly improve the high-temperature oxidation resistance of the Ti6Al4V alloy.

The XRD patterns of the oxidized surface of the coatings are shown in Figure 8. The results indicate that all phases on the surface of the HEA coatings are composed of various types of oxides. For the CoCrCuFeNi HEA coating, the surface oxides include CuO, $TiO_2$, $Fe_3O_4$, and $Cr_2O_3$. As the Al content increases, the intensity of the CuO peak decreases, and the $Al_2O_3$ phase appears on the oxidized surface of the coating. Moreover, the peak intensity of $Al_2O_3$ and $Cr_2O_3$ increases with a higher Al content. For the $Cu_{1.0}$, $Cu_{0.7}Al_{0.3}$, and $Cu_{0.5}Al_{0.5}$, the surface oxides are primarily CuO, $Fe_3O_4$, and $TiO_2$, while the surface oxides of the $Cu_{0.3}Al_{0.7}$ and $Al_{1.0}$ coatings are mainly $Cr_2O_3$ and $Al_2O_3$. With the increase in the Al content, the peak intensity of $Al_2O_3$ and $Cr_2O_3$ is gradually enhanced. This suggests that the addition of Al elements promotes the formation of $Al_2O_3$ and $Cr_2O_3$ on the surface of the HEA coatings. The presence of $Al_2O_3$ and $Cr_2O_3$ in the oxide layer increases the surface density of the HEA coatings, effectively preventing the inward diffusion of oxygen and slowing down the oxidation process.

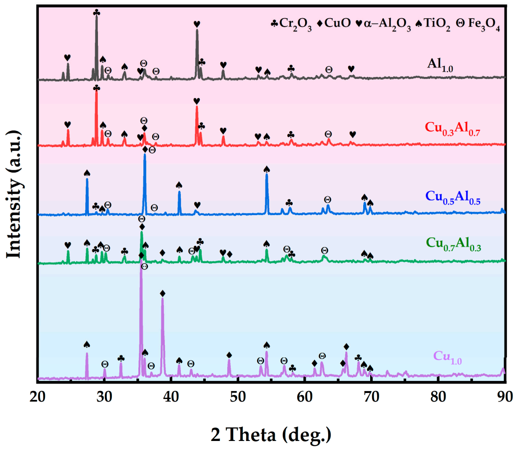

**Figure 8.** XRD patterns of $Al_xCoCrCu_yFeNi$ HEA coatings post-oxidation test.

Figure 9 shows the surface morphology of the coatings after 50 h of oxidation at 800 °C, while Figure 10 presents the cross-sectional morphology and elemental distribution of the coatings. The strong bonding between the oxide layer and the substrate, without any peeling phenomenon observed, indicates a robust bonding strength at the interface. In contrast, the Ti6Al4V alloy substrate experiences severe surface oxidation, leading to a very loose and flaky oxide film, which will not be discussed further. The results show that the upper layer of the surface oxide is rich in Fe, Ti, and Cr, while the lower layer has a horizontal boundary rich in Ni and Co. During the oxidation process, Ni and Co in the oxide film diffuse and concentrate internally, forming a transition zone with a high concentration of these elements. The preferentially oxidized elements diffuse to the surface, where they combine with oxygen to form an oxide layer, while the remaining elements, such as Ni and Co, diffuse inward, aggregating to form a transition layer [2]. The diffusion rates of elements from highest to lowest are as follows: Ti, Cr, Co, and Ni [49,50]. Based on these diffusion rates, it can be inferred that Ti and Cr will diffuse more quickly than Co and Ni, leading to their preferential reaction with oxygen to form oxides. On the other hand, Co and Ni are slower to oxidize and, therefore, accumulate inward, contributing to the formation of the transition layer. This transition layer not only hinders the diffusion of elements from the coating to the surface but also prevents the inward diffusion of oxygen atoms, thereby enhancing the coating's high-temperature oxidation resistance and protecting the Ti6Al4V alloy substrate.

The likelihood of each element reacting with oxygen can be determined by analyzing the change in Gibbs free energy with temperature. From a thermodynamic perspective, the more negative the value of the Gibbs free energy, the more the reaction is thermodynamically favored, and thus, the more likely the reaction will occur [51], Figure 11 shows the Gibbs free energy of each oxidation product in these high-entropy alloys at different temperatures. The surface oxides of the $Cu_{1.0}$ coating (Figures 9a and 10a) are mainly composed of CuO, $Fe_3O_4$, and $TiO_2$. As can be seen from Figure 9a, the primary reason for this phenomenon is the distribution of $TiO_2$ within the oxide layer, which creates significant gaps between the layers. These gaps provide channels for the rapid diffusion of oxygen, adversely affecting the oxidation resistance of the coating at high temperatures. In addition, the oxide layer is loosely arranged, and several diffused voids can be seen in the oxidation cross-section. This loose structure aggravates the oxidation process and results in the formation of a thicker oxidation layer. Compared to the $Cu_{1.0}$ coating, the oxidized surface of the $Cu_{0.7}Al_{0.3}$ coating shows significant changes following the addition of Al. The oxide morphology transitions from larger blocks to smaller plate-like structures (Figure 9b), and the oxide layer becomes denser and thinner. As can be seen from Figure 10b, $TiO_2$ is mainly concentrated in the outermost layer of the oxide layer, while Ni and Co are enriched in the innermost layer to form a horizontal transition zone. Other elements are evenly distributed, and the contents of CuO and $Fe_3O_4$ decrease, which aligns with XRD results. Based on the XRD analysis, it can be seen that the addition of Al leads to the formation of a certain amount of $Al_2O_3$ on the oxidized surface. Al easily reacts with oxygen at high temperatures to form a continuous and dense $Al_2O_3$ film, which effectively prevents high-temperature oxidation of the Ti6Al4V alloy substrate. However, there are still some voids in the oxide layer, resulting in a relatively thick oxide film. Compared with the $Cu_{1.0}$ and $Cu_{0.7}Al_{0.3}$ coatings, the $Cu_{0.5}Al_{0.5}$ and $Cu_{0.3}Al_{0.7}$ coatings have a more dense surface oxide film distribution and no obvious porosity (Figure 9c,d). The cross-section of the oxide layer is uniform and dense, showing no significant voids or holes, and the thickness of the oxide layer decreased significantly (Figure 10c,d). It is worth mentioning that for the $Cu_{0.3}Al_{0.7}$ coating, which contains a higher Al content, it can be seen that the concentration of $Al_2O_3$ and $Cr_2O_3$ increases. $Al_2O_3$ is primarily concentrated in the innermost layer. This can be attributed to the high diffusion coefficient of Al and the relatively low bond energy between Al and oxygen compared to other elements, making Al preferentially oxidize at the surface of the coating and form a dense $Al_2O_3$ film. This $Al_2O_3$ layer provides effective protection for the coating at an early stage [50]. As oxidation progresses, Cr diffuses outward through the pores at the interface between the $Al_2O_3$ layer and the coating–oxide boundary, and the $Cr_2O_3$-rich oxide protective film formed in the steady state phase further impedes the diffusion of oxygen, preventing the formation of new oxides with other elements. For the $Al_{1.0}$ coating, which has the highest Al content, the $Al_2O_3$ film generated during the oxidation process is denser and more concentrated. At the same time, the higher content of $Cr_2O_3$ oxides also provides better protection for the coating. As can be seen from Figure 10e, the oxide layer is the thinnest and densest, offering superior protection compared to the Ti6Al4V alloy substrate, which further improves the oxidation resistance at high temperatures.

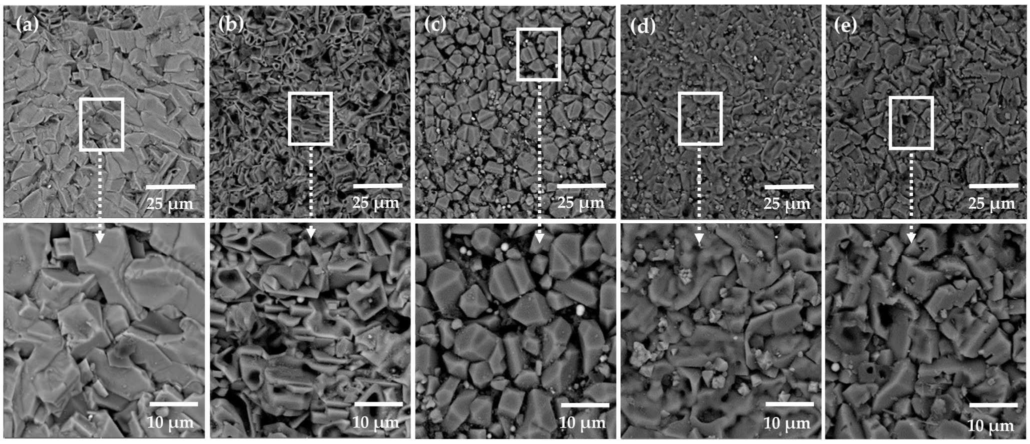

**Figure 9.** The SEM images of the oxidized surface of $Al_xCoCrCu_yFeNi$ HEA coatings post-oxidation test at 800 °C for 50 h: (**a**) $Cu_{1.0}$; (**b**) $Cu_{0.3}Al_{0.7}$; (**c**) $Cu_{0.5}Al_{0.5}$; (**d**) $Cu_{0.3}Al_{0.7}$; (**e**) $Al_{1.0}$.

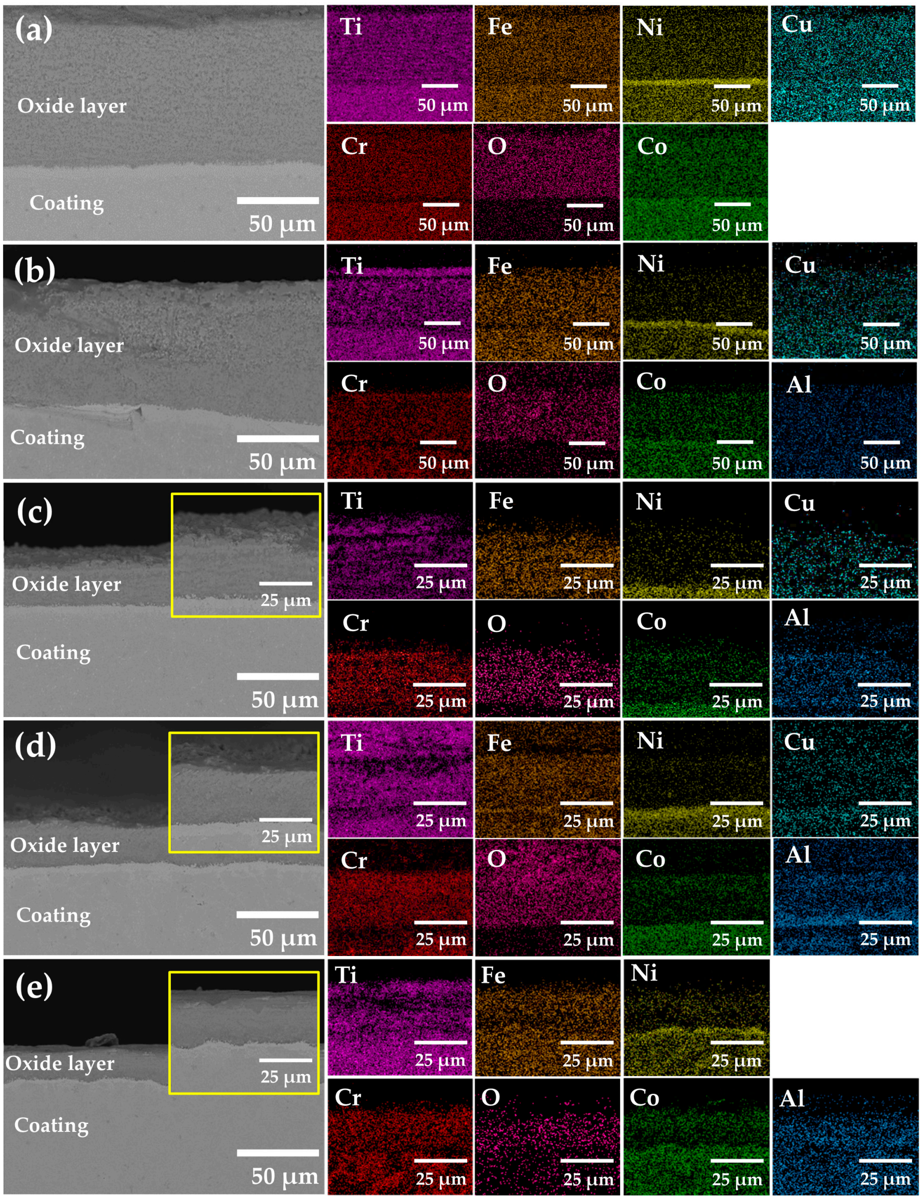

**Figure 10.** The SEM images and corresponding EDS mappings of the oxidation scale of $Al_xCoCrCu_yFeNi$ HEA coatings at 800 °C for 50 h: (**a**) $Cu_{1.0}$; (**b**) $Cu_{0.7}Al_{0.3}$; (**c**) $Cu_{0.5}Al_{0.5}$; (**d**) $Cu_{0.3}Al_{0.7}$; (**e**) $Al_{1.0}$.

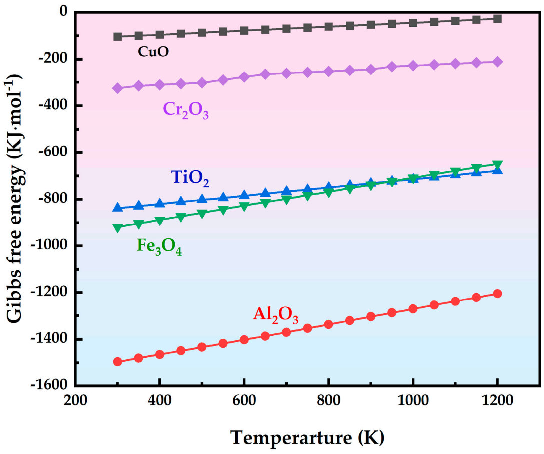

**Figure 11.** Gibbs free energy of CuO, $Cr_2O_3$, $TiO_2$, $Fe_3O_4$, and $Al_2O_3$ with temperature.

The oxidation mechanism of the coatings for $Cu_{1.0}$, $Cu_{0.5}Al_{0.5}$, and $Al_{1.0}$ is illustrated in Figure 12. During the initial stage of oxidation, the oxidation reaction is mainly dominated by the reaction rate of the coating surface, where the alloying elements and oxygen are more readily available for the oxidation process. According to the thermodynamic principle, the larger the absolute value of the Gibbs free energy, the more significant the tendency of the elements to undergo spontaneous reaction. As the oxidation process progresses, after a certain length of time, the elements involved in the oxidation at the surface of the coating become increasingly depleted. During this period, the oxidation behavior is largely controlled by the diffusion rates of alloying elements outward from the coating and the rate of oxygen diffusion inward. Therefore, the formation of the final oxidation products is predominantly attributed to the composition of the alloying elements in the coating during the slower oxidation phase, as well as their oxidation kinetics. In this process, oxygen and metal cations within the coating interact to form oxides, with the higher the content of alloying elements and the faster the diffusion rates. The higher the content of alloying elements and the faster their diffusion rates, the more likely the elements are to preferentially react with oxygen and form an oxide layer on the surface of the coating. This oxide layer plays a critical role in protecting the substrate, significantly influencing the overall performance of the coating as well as the evolution of the subsequent oxidation process.

At the early stage of oxidation, which is characterized by rapid oxidation, Fe has high reactivity with O. During this period, Fe fully reacts with O, and as oxidation proceeds, $Fe_3O_4$ oxide is generated. However, the structure of this oxide is extremely loose, which allows for relatively easy atomic diffusion and does not effectively prevent the inward diffusion of oxygen. Ti atoms, due to their relatively large atomic radius and strong binding affinity with other elements, require the surmounting of a certain energy barrier for lattice diffusion. Consequently, their diffusion is somewhat inhibited, leading to the formation of $TiO_2$ on the coating surface in a more dispersed, lamellar distribution. The diffusion of Cr contributes to the formation of a continuous and dense oxide film, which can play a certain protective effect on the substrate. The Cr-Fe phase composed of the BCC phase structure at the grain boundary is enriched with a large amount of Cr, attaining a high concentration. Moreover, the atomic arrangement at the grain boundaries is relatively disordered, and the migratory activation energy of atoms is relatively low, which favors the diffusion of Cr atoms and thus promotes the production of a relatively dense $Cr_2O_3$. In addition, in the alloy with a higher Cu content (Figure 12a, b), the phenomenon that Cu tends to aggregate at the grain boundaries leads to the formation of more CuO. However, this oxide exists in a loose arrangement and diffuse distribution, which cannot effectively limit the mutual diffusion of the atoms, resulting in a relatively thick oxide layer. Compared with other elements, the diffusion rate of Co and Ni is relatively low. As a result, during the oxidation process, they are unable to react with oxygen on time and instead aggregate in the inner layer to form a transition layer. Al has the lowest Gibbs free energy and the fastest diffusion coefficient, so it can combine with oxygen at a very fast rate and preferentially form an $Al_2O_3$ oxidized layer on the surface of the alloy. When the content of Al is relatively low (Figure 12b), the formed $Al_2O_3$ oxide film is discontinuous and low in density, which has a limited inhibitory effect in inhibiting atomic diffusion. With the increase in the Al content (Figure 12c), a layer with a uniform and continuous distribution of $Al_2O_3$ film is formed on the surface of the alloy. This continuous oxide layer serves as a barrier, effectively isolating the substrate from external oxygen atoms and preventing further reactions between oxygen and other elements. This enhances the antioxidant performance and reduces the thickness of the oxidized layer.

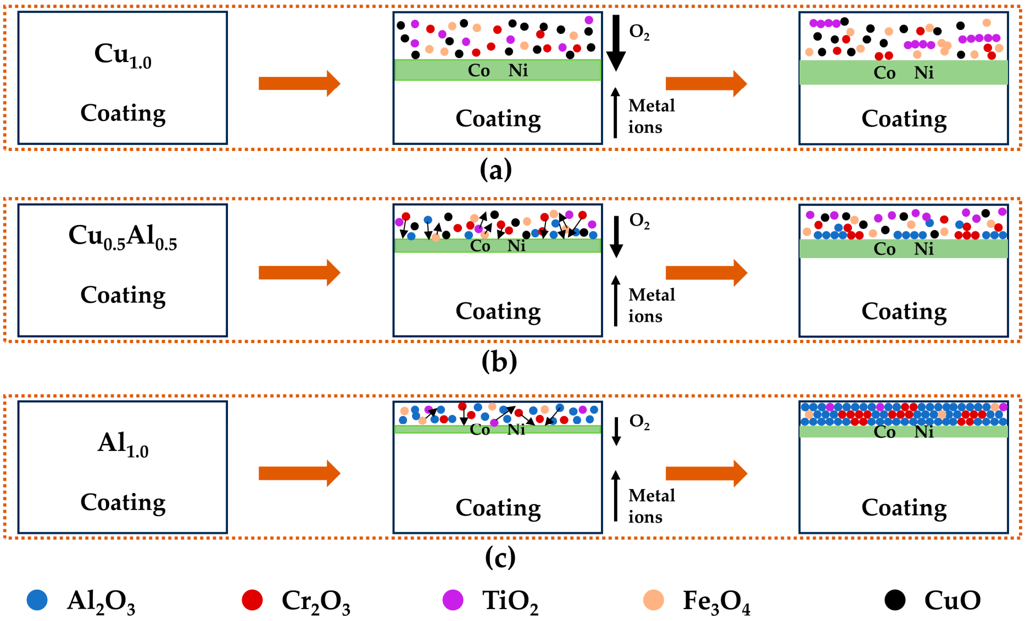

**Figure 12.** Schematic description of high-temperature oxidation of coatings [36]: (**a**) $Cu_{1.0}$; (**b**) $Cu_{0.5}Al_{0.5}$; (**c**) $Al_{1.0}$.

## 4. Conclusions

$Al_xCoCrCu_yFeNi$ HEA coatings were fabricated on the surface of a Ti6Al4V alloy using laser cladding technology. The influence of the Al/Cu ratio on the microstructure and high-temperature oxidation resistance of the $Al_xCoCrCu_yFeNi$ HEA coatings was thoroughly analyzed. The main conclusions drawn from this study are as follows.

- The coatings are primarily composed of FCC, BCC, and Ti-rich Laves-reinforced phases. The $Cu_{1.0}$ coating exhibits Co-Ni-Ti-rich FCC phases in the dendrites, Fe-Cr-rich BCC phases in the inter-dendrite regions, and Cu is concentrated at the grain boundaries to form Cu-rich phases (FCC2). The amount of Cu-rich phases decreases as the Cu content is reduced, and the FCC2 phases completely disappear when the Al content reaches 1.0. With the increase in the Al content, the negative mixing enthalpy between Ti and Al causes the FCC1 phases to transition from Co-Ni-Ti-rich to $AlNi_2Ti$- or $AlCo_2Ti$-rich phases.
- Compared to the Ti6Al4V alloy substrate, the solid solution strengthening induced by the doping of elements with larger atomic radii in the high-entropy alloy coatings, as well as the precipitation strengthening effect resulting from the diffusion of Ti from the

substrate into the coatings, significantly increases the microhardness of the coatings. The microhardness of the $Al_xCoCrCu_yFeNi$ HEA coatings is 2.01, 2.06, 2.08, 2.09, and 2.11 times that of the Ti6Al4V alloy substrate, respectively.

- The high-temperature oxidation resistance of the coating increases with the Al content, and the high-temperature oxidation resistance of the $Al_xCoCrCu_yFeNi$ HEA coating is the best when x = 1.0. The oxidation weight gain is 0.098 $mg \cdot mm^{-2}$, which is only 35% of that observed for the Ti6Al4V alloy substrate. The Al element easily reacts with oxygen to generate a continuous and dense $Al_2O_3$ film under high-temperature conditions, effectively preventing the high-temperature oxidation behavior of the substrate. Additionally, Cr atoms diffuse outward through the pores at the interface between the $Al_2O_3$ layer and the substrate, as well as through the oxide layer, promoting the formation of $Cr_2O_3$. As oxidation progresses, the formation of a $Cr_2O_3$-rich oxide layer in the steady-state stage impedes the further oxidation of the coating.

**Author Contributions:** L.Z.: Conceptualization, methodology, and writing—original draft. H.L.: Supervision, funding acquisition, and project administration. Q.Z.: Data curation. J.L.: Visualization. Y.P.: Investigation. X.H.: Formal analysis and investigation. C.Y.: Software. Y.L.: Data curation. Y.W.: Visualization. All authors have read and agreed to the published version of the manuscript.

**Funding:** This research was jointly supported financially by the National Nature Science Foundation of China (Grant No. 52475192), the Yunnan Fundamental Research Projects (Grant No. 202201AS070035), and the Scientific and Technologies Project of Yunnan Precious Metals Laboratory (YPML-20240502004, YPML-20240502080).

**Data Availability Statement:** Data will be made available on request.

**Acknowledgments:** The authors extend their appreciation to the China–Ukraine Institute of Welding of Guangdong Academy of Sciences, for providing equipment support, and Ben Niu for his valuable support throughout this project.

**Conflicts of Interest:** The authors declare that they have no known competing financial interests or personal relationships that could have appeared to influence the work reported in this paper.

## References

1. Kumar, A.; Singh, G. Surface modification of Ti6Al4V alloy via advanced coatings: Mechanical, tribological, corrosion, wetting, and biocompatibility studies. *J. Alloys Compd.* **2024**, *989*, 174418. [CrossRef]
2. Li, S.; Yamaguchi, T. High-temperature oxidation performance of laser-cladded amorphous TiNiSiCrCoAl high-entropy alloy coating on Ti-6Al-4V surface. *Surf. Coat. Technol.* **2022**, *433*, 128123. [CrossRef]
3. Zhang, K.; Li, B.; Liu, W.; Liu, W.; Wang, W.; Wang, H.; Bian, H. Influences of friction stir processing on the microstructure and properties of TC4 titanium alloy by laser metal deposition. *J. Alloys Compd.* **2024**, *1008*, 176769. [CrossRef]
4. Han, X.; Ma, J.; Tian, A.; Wang, Y.; Li, Y.; Dong, B.; Tong, X.; Ma, X. Surface modification techniques of titanium and titanium alloys for biomedical orthopaedics applications: A review. *Colloids Surf. B Biointerfaces* **2023**, *227*, 113339. [CrossRef]
5. Ren, Y.; Wu, H.; Liu, B.; Liu, Y.; Guo, S.; Jiao, Z.B.; Baker, I. A comparative study on microstructure, nanomechanical and corrosion behaviors of AlCoCuFeNi high entropy alloys fabricated by selective laser melting and laser metal deposition. *J. Mater. Sci. Technol.* **2022**, *131*, 221–230. [CrossRef]
6. Xie, Y.; Wen, X.; Yan, J.; Huang, B.; Zhuang, J. Microstructure and wear resistance of AlCoCrFeNiCuSnX high-entropy alloy coatings by plasma cladding. *Vacuum* **2023**, *214*, 112176. [CrossRef]
7. Korobov, Y.; Antonov, M.; Astafiev, V.; Brodova, I.; Kutaev, V.; Estemirova, S.; Devyatyarov, M.; Okulov, A. Erosion Wear Behavior of HVAF-Sprayed $WC/Cr_3C_2$-Based Cermet and Martensitic Stainless Steel Coatings on AlSi7Mg0.3 Alloy: A Comparative Study. *J. Manuf. Mater. Process* **2024**, *8*, 231. [CrossRef]
8. Qadir, D.; Sharif, R.; Nasir, R.; Awad, A.; Mannan, H.A. A review on coatings through thermal spraying. *Chem. Pap.* **2023**, *78*, 71–91. [CrossRef]
9. Ahmed, A.; Mhaede, M.; Wollmann, M.; Wagner, L. Characteristics of sintered HA coating deposited by chemical method on AISI 316L substrate. *Mater. Des.* **2015**, *76*, 9–17. [CrossRef]

10. He, X.; Zhang, H.; Wu, Y.; Yang, T.; Li, R.; Nong, Z.; Cui, X. Research progress on effects of additives and pre- and post-treatment processes on corrosion resistance of micro-arc oxidation coatings on titanium and its alloys. *Int. J. Electrochem. Sci.* **2024**, *19*, 100836. [CrossRef]
11. Wu, H.; Wu, Y.; Yan, M.; Tu, B.; Li, Y. Microstructure and mechanical properties of surface coating prepared on grade 2 titanium by Ni-B composite electroplating and laser cladding. *Opt. Laser Technol.* **2023**, *164*, 109498. [CrossRef]
12. Xiang, Y.; Zou, C. Effect of Arc Currents on the Mechanical, High Temperature Oxidation and Corrosion Properties of CrSiN Nanocomposite Coatings. *Coatings* **2021**, *12*, 40. [CrossRef]
13. Ma, Q.; Zhang, H.; Lv, Y.; Song, C.; Guo, N.; Xiao, G.; Zhao, W. Microstructure and properties of $W_{0.5}Ta_{0.3}MoNbVAlTi_{1\text{-}x}Zr_x$ high entropy alloy coatings by laser cladding on the surface of 45# steel. *Ceram. Int.* **2023**, *49*, 36416–36428. [CrossRef]
14. Zhu, L.; Xue, P.; Lan, Q.; Meng, G.; Ren, Y.; Yang, Z.; Xu, P.; Liu, Z. Recent research and development status of laser cladding: A review. *Opt. Laser Technol.* **2021**, *138*, 106915. [CrossRef]
15. Zhao, H.; Zhao, C.; Xie, W.; Wu, D.; Du, B.; Zhang, X.; Wen, M.; Ma, R.; Li, R.; Jiao, J.; et al. Research Progress of Laser Cladding on the Surface of Titanium and Its Alloys. *Materials* **2023**, *16*, 3250. [CrossRef]
16. Zhang, Y.; Liu, Z.; Lv, Z.; Cao, J.; Tong, Y.; Sun, M.; Cui, C.; Wang, X. Effect of SiC and TiC content on microstructure and wear behavior of Ni-based composite coating manufactured by laser cladding on Ti–6Al–4V. *Wear* **2024**, *552–553*, 205431. [CrossRef]
17. Meng, Q.; Geng, L.; Ni, D. Laser cladding NiCoCrAlY coating on Ti-6Al-4V. *Mater. Lett.* **2005**, *59*, 2774–2777. [CrossRef]
18. Liu, X.-B.; Yu, R.-L. Microstructure and high-temperature wear and oxidation resistance of laser clad $\gamma/W_2C/TiC$ composite coatings on $\gamma$-TiAl intermetallic alloy. *J. Alloys Compd.* **2007**, *439*, 279–286. [CrossRef]
19. Kooi, B.J.; Pei, Y.T.; De Hosson, J.T.M. The evolution of microstructure in a laser clad TiB–Ti composite coating. *Acta Mater.* **2003**, *51*, 831–845. [CrossRef]
20. Barbatti, C.; Garcia, J.; Brito, P.; Pyzalla, A.R. Influence of WC replacement by TiC and (Ta,Nb)C on the oxidation resistance of Co-based cemented carbides. *Int. J. Refract. Met. Hard Mat.* **2009**, *27*, 768–776. [CrossRef]
21. Yang, X.; Wang, L.; Gao, Z.; Wang, Q.; Du, M.; Zhan, X. WC distribution, microstructure evolution mechanism and microhardness of a developed Ti-6Al-4 V/WC MMC coating fabricated by laser cladding. *Opt. Laser Technol.* **2022**, *153*, 108232. [CrossRef]
22. Li, J.; Cui, X.; Guan, Y.; Wan, S.; Jin, G.; Zheng, W.; Su, W. Enhancing coating performance: Design and characterization of a Ti-Al-Si-Cr-SiC system coating using ultrasonic and rare earth assisted laser cladding. *Mater. Charact.* **2024**, *210*, 113823. [CrossRef]
23. Das, A.K. Effect of rare earth oxide additive in coating deposited by laser cladding: A review. *Mater. Today Proc.* **2022**, *52*, 1558–1564. [CrossRef]
24. Yeh, J.-W.; Chen, S.-K.; Lin, S.-J.; Gan, J.-Y.; Chin, T.-S.; Shun, T.-T.; Tsau, C.-H.; Chang, S.-Y. Nanostructured High-Entropy Alloys with Multiple Principal Elements: Novel Alloy Design Concepts and Outcomes. *Adv. Eng. Mater.* **2004**, *6*, 299–303. [CrossRef]
25. Diao, H.Y.; Feng, R.; Dahmen, K.A.; Liaw, P.K. Fundamental deformation behavior in high-entropy alloys: An overview. *Curr. Opin. Solid State Mat. Sci.* **2017**, *21*, 252–266. [CrossRef]
26. Tokarewicz, M.; Grądzka-Dahlke, M. Review of Recent Research on AlCoCrFeNi High-Entropy Alloy. *Metals* **2021**, *11*, 1302. [CrossRef]
27. Dąbrowa, J.; Cieślak, G.; Stygar, M.; Mroczka, K.; Berent, K.; Kulik, T.; Danielewski, M. Influence of Cu content on high temperature oxidation behavior of AlCoCrCuxFeNi high entropy alloys (x = 0; 0.5; 1). *Intermetallics* **2017**, *84*, 52–61. [CrossRef]
28. Guo, S.; Liu, C.T. Phase stability in high entropy alloys: Formation of solid-solution phase or amorphous phase. *Prog. Nat. Sci. Mater. Int.* **2011**, *21*, 433–446. [CrossRef]
29. Miracle, D.B.; Senkov, O.N. A critical review of high entropy alloys and related concepts. *Acta Mater.* **2017**, *122*, 448–511. [CrossRef]
30. Du, X.; Du, Z.; Cao, J.; Zhang, S.; Gong, T.; Sun, B.; Zhang, C.; Huo, R.; Liu, J.; Cheng, J. Enhance the mechanical properties of CoCrFeNi high entropy alloy: Rare-earth element Gd was employed as a "cladding structure" to refine grains. *Mater. Today Commun.* **2024**, *41*, 110732. [CrossRef]
31. Zhang, S.; Sun, Y.; Cheng, W.; Chen, Y.; Gu, J. High temperature oxidation behavior of CoCrFeNiMo0.2 high-entropy alloy coatings produced by laser cladding. *Mater. Today Commun.* **2024**, *39*, 108639. [CrossRef]
32. Zhu, Z.-X.; Liu, X.-B.; Liu, Y.-F.; Zhang, S.-Y.; Meng, Y.; Zhou, H.-B.; Zhang, S.-H. Effects of Cu/Si on the microstructure and tribological properties of FeCoCrNi high entropy alloy coating by laser cladding. *Wear* **2023**, *512–513*, 204533. [CrossRef]
33. Ye, Y.F.; Wang, Q.; Lu, J.; Liu, C.T.; Yang, Y. High-entropy alloy: Challenges and prospects. *Mater. Today* **2016**, *19*, 349–362. [CrossRef]
34. Butler, T.M.; Weaver, M.L. Oxidation behavior of arc melted AlCoCrFeNi multi-component high-entropy alloys. *J. Alloys Compd.* **2016**, *674*, 229–244. [CrossRef]
35. Qin, L.; Ren, P.; Yi, Y.; Xie, T.; Hu, Y.; Chen, D.; Zhou, S. Effect of $Al_2O_3$ content on the high-temperature oxidation behaviour of CoCrAlYTa coatings produced by laser-induction hybrid cladding. *Corros. Sci.* **2022**, *209*, 110739. [CrossRef]
36. Wang, S.; Chen, Z.; Zhang, P.; Zhang, K.; Chen, C.L.; Shen, B.L. Influence of Al content on high temperature oxidation behavior of $Al_xCoCrFeNiTi_{0.5}$ high entropy alloys. *Vacuum* **2019**, *163*, 263–268. [CrossRef]

37. Huang, C.; Zhang, Y.; Shen, J.; Vilar, R. Thermal stability and oxidation resistance of laser clad TiVCrAlSi high entropy alloy coatings on Ti–6Al–4V alloy. *Surf. Coat. Technol.* **2011**, *206*, 1389–1395. [CrossRef]
38. Zhang, H.X.; Dai, J.J.; Sun, C.X.; Li, S.Y. Microstructure and wear resistance of TiAlNiSiV high-entropy laser cladding coating on Ti-6Al-4V. *J. Mater. Process. Technol.* **2020**, *282*, 116671. [CrossRef]
39. Geng, H.; Shen, J.; Hu, S.; Zhang, F.; Geng, K. Microstructure, corrosion and wear behavior of $(AlCu)_{3.5}$CoCrNiFe and $(AlCu)_{3.5}$CoCrNiTi high entropy alloy coatings prepared by laser cladding on AZ91 magnesium alloy. *J. Mater. Process Technol.* **2024**, *30*, 3383–3393. [CrossRef]
40. Yeh, J.-W.; Chang, S.-Y.; Hong, Y.-D.; Chen, S.-K.; Lin, S.-J. Anomalous decrease in X-ray diffraction intensities of Cu–Ni–Al–Co–Cr–Fe–Si alloy systems with multi-principal elements. *Mater. Chem. Phys.* **2007**, *103*, 41–46. [CrossRef]
41. Li, Y.; Shi, Y. Phase assemblage and properties of laser cladded TixCrFeCoNiCu high-entropy alloy coating on aluminum. *Mater. Res. Express* **2020**, *7*, 036519. [CrossRef]
42. Hao, X.; Liu, H.; Zhang, X.; Tao, J.; Wang, Y.; Yang, C.; Liu, Y. Microstructure and wear resistance of in-situ TiN/$(Nb, Ti)_5Si_3$ reinforced MoNbTaWTi-based refractory high entropy alloy composite coatings by laser cladding. *Appl. Surf. Sci.* **2023**, *626*, 157240. [CrossRef]
43. Jiang, Y.Q.; Li, J.; Juan, Y.F.; Lu, Z.J.; Jia, W.L. Evolution in microstructure and corrosion behavior of $AlCoCr_xFeNi$ high-entropy alloy coatings fabricated by laser cladding. *J. Alloys Compd.* **2019**, *775*, 1–14. [CrossRef]
44. Huang, Y. Characterization of dilution action in laser-induction hybrid cladding. *Opt. Laser Technol.* **2011**, *43*, 965–973. [CrossRef]
45. Li, K.; Chen, W. Recent progress in high-entropy alloys for catalysts: Synthesis, applications, and prospects. *Mater. Today Energy* **2021**, *20*, 100638. [CrossRef]
46. Yi, H.; Yang, X.; Yang, Y.; Yin, B.; Hu, J.; Liang, M.; Yue, J.; Yin, F. New insights in the oxidation behavior of $(FeCoCrNi)_{94}Al_4Ti_2Si$ high entropy alloys at 1100 °C. *Corros. Sci.* **2024**, *227*, 111673. [CrossRef]
47. Yu, K.; Zhao, W.; Li, Z.; Guo, N.; Xiao, G.; Zhang, H. High-temperature oxidation behavior and corrosion resistance of in-situ TiC and Mo reinforced AlCoCrFeNi-based high entropy alloy coatings by laser cladding. *Ceram. Int.* **2023**, *49*, 10151–10164. [CrossRef]
48. Chen, G.; Yang, H.; Sun, H.; Wang, F.; Wang, H.; Kong, Q.; An, X.; Zhang, Y.; Wang, J. Exploring the high-temperature steam oxidation behaviors of the lean-Cr (7–10 wt%) FeCrAl alloys. *Corros. Sci.* **2022**, *194*, 109927. [CrossRef]
49. Tsai, K.Y.; Tsai, M.H.; Yeh, J.W. Sluggish diffusion in Co–Cr–Fe–Mn–Ni high-entropy alloys. *Acta Mater.* **2013**, *61*, 4887–4897. [CrossRef]
50. Dąbrowa, J.; Kucza, W.; Cieślak, G.; Kulik, T.; Danielewski, M.; Yeh, J.-W. Interdiffusion in the FCC-structured Al-Co-Cr-Fe-Ni high entropy alloys: Experimental studies and numerical simulations. *J. Alloys Compd.* **2016**, *674*, 455–462. [CrossRef]
51. Sun, D.; Cai, Y.; Zhu, L.; Gao, F.; Shan, M.; Manladan, S.M.; Geng, K.; Han, J.; Jiang, Z. High-temperature oxidation and wear properties of TiC-reinforced CrMnFeCoNi high entropy alloy composite coatings produced by laser cladding. *Surf. Coat. Technol.* **2022**, *438*, 128407. [CrossRef]